Research in Astronomy and Astrophysics, 25:015002 (8pp), 2025 January

https://doi.org/10.1088/1674-4527/ad981b
CSTR: 32081.14.RAA.ad981b

Timing Calibration of the Follow-up X-Ray Telescope On Board the Einstein Probe Satellite

Xiaofan Zhao[1], Weiwei Cui[1], Hao Wang[1], Yifan Zhang[1,2], Zijian Zhao[1,2], Dongjie Hou[1], Yuxuan Zhu[1], Yusa Wang[1], Jingjing Xu[1], Laidan Luo[1], Dawei Han[1], Yanji Yang[1], Juan Wang[1], Jia Ma[1], Xiongtao Yang[1], Jia Huo[1], Wei Li[1], Ziliang Zhang[1], Haoyang Geng[1], and Yong Chen[1]

[1] Key Laboratory of Particle Astrophysics, Institute of High Energy Physics, Chinese Academy of Sciences, Beijing 100049, China; zhaoxf@ihep.ac.cn, ychen@ihep.ac.cn

[2] University of Chinese Academy of Sciences, Chinese Academy of Sciences, Beijing 100049, China

Received 2024 September 03; revised 2024 November 03; accepted 2024 November 20; published 2024 December 31

Abstract

The Follow-up X-ray Telescope (FXT) is one of the main scientific instruments on board the Einstein Probe astronomical satellite, which was launched in 2024 January. FXT consists of two Wolter I type nested telescopes (FXT-A and FXT-B) with a focal length of 1600 mm. The focal plane detector employs a PNCCD with 384×384 pixels. The timing mode of FXT serves as the primary operating mode for fast X-ray timing observations. To evaluate and validate the timing performance of FXT prior to launch, a comprehensive timing calibration was performed at the 100 m X-ray test facility. By simulating various periodic Crab-like profiles using the Grid Controlled X-ray Tube (GCXT) in conjunction with a pulsar simulation module, it was verified that the relative time accuracy of FXT exceeds 5×10^{-9}. Furthermore, employing GCXT with a voltage pulse generation module enabled the determination of the time resolutions for FXT-A and FXT-B, recorded as 45.6 ± 2.7 μs and 47.1 ± 2.8 μs, respectively. An absolute timing calibration for FXT-B was carried out using the GCXT and a time interval analyzer, revealing a measured time delay of 3.9 ± 2.1 μs for FXT-B.

Key words: telescopes – instrumentation: detectors – methods: data analysis

1. Introduction

The Einstein Probe (EP) satellite is a time-domain X-ray astronomical mission (Yuan et al. 2018), which was successfully launched in 2024 January with an altitude of 600 km and an inclination of 29°. The primary science objectives of EP include the discovery and characterization of cosmic X-ray transients and burst sources, as well as the search for X-ray sources associated with gravitational-wave events (Yuan et al. 2024). EP comprises two kinds of scientific payloads: the Wide-field X-ray Telescope (WXT) and the Follow-up X-ray Telescope (FXT). WXT is equipped with 12 lobster-eye telescopes, providing a wide field of view that covers over 3800 square degrees, which allows for the detection of X-ray transients and burst sources (Zhao et al. 2018; Chen et al. 2022). FXT consists of 2 Wolter I type nested telescopes (FXT-A and FXT-B), featuring a narrow field of view of 1 square degree (Chen et al. 2020; Yang et al. 2023; Friedrich et al. 2024). FXT mainly conducts follow-up observations of transients and burst sources triggered by WXT. Additionally, FXT conducts sky survey observations and target-of-opportunity observations.

The mirror assembly of FXT is similar to that of eROSITA in design (Friedrich et al. 2008; Arcangeli et al. 2017; Sunyaev et al. 2021). The mirror assembly for FXT-A is provided by the European Space Agency (ESA), while the mirror assembly for FXT-B is the flight spare mirror of eROSITA provided by the Max Planck Institute for Extraterrestrial Physics (MPE). Each mirror assembly consists of 54 mirror shells with an outer diameter of 360 mm and a shared focal length of 1600 mm. The focal plane detector for each mirror assembly adopts a PNCCD provided by MPE (Meidinger et al. 2021). This detector is divided into two sections: the image area and the frame store area. Both the image area and the frame store area have 384×384 pixels. The pixel size in the image area is 75 μm $\times$ 75 μm, producing a 28.8 mm $\times$ 28.8 mm image area size. The pixels in the frame store area are shortened to 75 μm $\times$ 51 μm. FXT is optimized to focus photons in the 0.3–10 keV energy band. Additionally, FXT is designed to have three operating modes with different integration times and readout schemes depending on the scientific requirements of the astrophysical target. These modes are full-frame mode, partial-window mode, and timing mode (Cui et al. 2023; Zhao et al. 2024).

Fast X-ray timing observations are a critical aspect of the EP, with the timing mode serving as the primary operating mode for capturing rapid variability in astrophysical objects due to its high time resolution. Accurate timing calibration is essential for scientific investigations related to fast radio bursts

(Cordes & Chatterjee 2019), tidal disruption events (Gezari 2021), and millisecond pulsars (Harding 2022). To perform timing calibration for the timing mode, the Grid Controlled X-ray Tube (GCXT) with various driving modules is employed to generate X-ray pulses and simulate pulsar light curves (Zhou et al. 2013; Chen 2022). The GCXT has demonstrated success in timing calibration for GECAM (Li et al. 2020; Chen et al. 2021) and eXTP-SFA (Zhang et al. 2024), showcasing its excellent timing performance. Simulated pulsar light curves are instrumental in verifying the FXT's ability to detect pulsar profiles, while X-ray pulses are utilized to determine the time resolution and absolute timing of the FXT.

This paper is organized as follows: The timing system of the FXT and the experimental setup are detailed in Section 2 and Section 3, respectively. Section 4 focuses on the determination of FXT's time resolution. The capability of FXT to detect pulsar profiles is outlined in Section 5, followed by a discussion of the absolute timing calibration of FXT in Section 6. Finally, the conclusions are presented in Section 7.

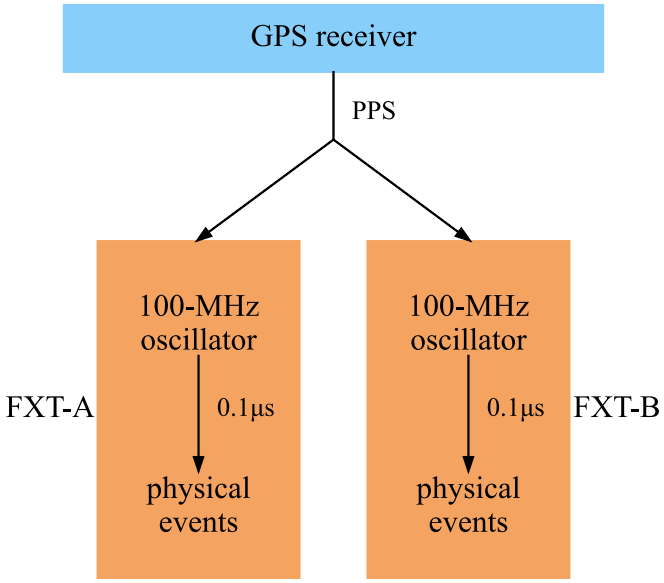

Figure 1. The schematic diagram of the timing system of FXT.

2. The Timing System of FXT

Similar to the timing systems of Insight-HXMT (Tuo et al. 2022) and GECAM (Xiao et al. 2022), EP combines local time and GPS Pulse Per Second (PPS) time to accurately determine the time of physical events detected by its detectors. EP is equipped with a GPS receiver that distributes the PPS signal to FXT, followed by a Coordinated Universal Time (UTC) event. The PPS and UTC events are stored together as a pair in the raw data package of FXT. Both FXT-A and FXT-B utilize independent 100 MHz temperature-compensated crystal oscillators to record local time for physical and PPS events with a high record time resolution of 0.1 μs. Figure 1 shows a schematic diagram of the timing system of FXT.

To compensate for time errors associated with PPS events and potential drifts in the temperature-compensated crystal oscillator, a linear function is employed to fit local time and PPS time for every 100 s. Figure 2 shows the fitting residuals for local time and PPS time over these intervals. The residuals are found to be less than 0.1 μs. To verify the accuracy of the timing system over long durations and at different temperatures, we conducted long-duration tests at various temperatures during thermal experiments. The results indicate that the fitting residuals remain below 0.1 μs under both long durations and varying temperatures, demonstrating that the FXT's timing system maintains high accuracy under these conditions.

3. Experimental Setup

3.1. Grid Controlled X-Ray Tube

To assess and verify the timing performance of FXT prior to launch, the GCXT equipped with a pulsar simulation module was utilized to generate simulated pulsar light curves based on input pulse profiles and periods. The design schematic of the setup is illustrated in Figure 3. A GPS-disciplined rubidium clock ensures long-term stability. The arbitrary function generator produces a waveform corresponding to the input period and profile, which drives the GCXT to produce the expected X-ray signal. The Crab Pulsar has been extensively utilized in timing calibration for numerous astronomical satellites (Kuiper et al. 2003; Rots et al. 2004; Terada et al. 2008; Molkov et al. 2010; Martin-Carrillo et al. 2012; Bachetti et al. 2021; Tuo et al. 2022; Xiao et al. 2022, 2024). Considering this, we generated simulated Crab-like profile light curves with varying periods using the GCXT.

In addition, X-ray pulses with a width of 2.8 μs were generated by the GCXT with a voltage pulse generation module to determine the time resolution and absolute timing. The function of the pulse signal generator (see Figure 3) is to produce narrow pulse signals that are fed into the GCXT, resulting in the emission of pulsed X-rays. Simultaneously, the time of the pulse signal is recorded to accurately ascertain the pulse time. The GCXT exhibits a time jitter of less than 0.2 μs and a time delay of less than 0.2 μs, ensuring precise timing performance (Chen 2022). The detailed performance specifications of the GCXT are summarized in Table 1.

The GCXT has been employed in the testing of the eXTP-SFA engineering model (Zhang et al. 2024). The eXTP-SFA detector utilizes a silicon drift detector (SDD) with a time resolution of better than 1 μs. Various simulated pulsar light curves with different profiles and periods have been tested using the SDD. Figure 4 presents the detected profile of the SDD in response to an input signal featuring a Crab-like profile with a period of 1 ms. The detected pulse profile closely

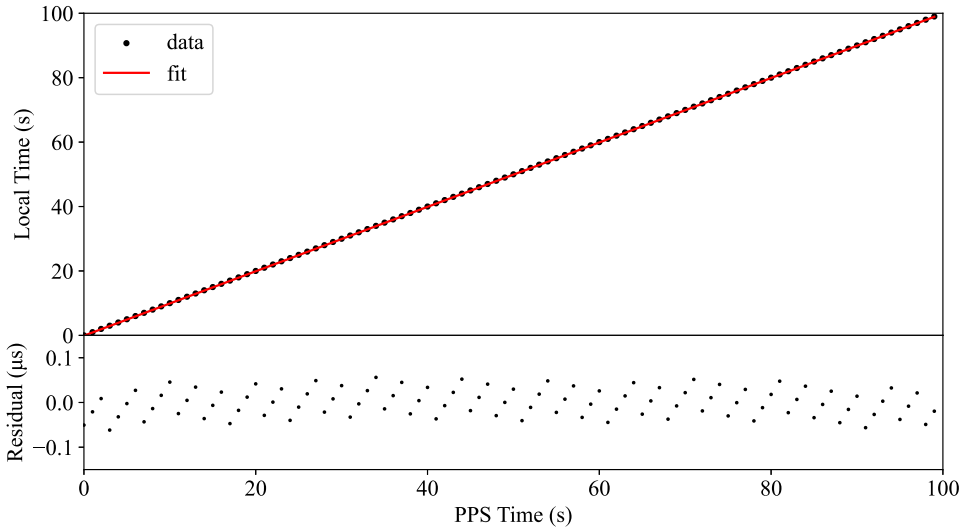

Figure 2. The residuals for a linear fit between local time and PPS time over 100 s. The fitting residuals remain below 0.1 μs under both long durations and varying temperatures.

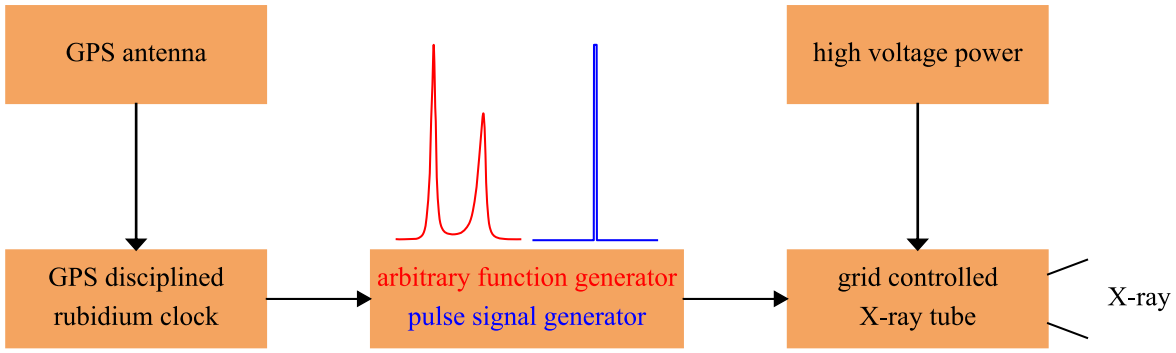

Figure 3. The design schematic diagram of GCXT. The pulsar simulation module (highlighted in red) includes an arbitrary function generator responsible for producing the waveform based on the input period and profile. In contrast, the voltage pulse generation module (highlighted in blue) includes a pulse signal generator that produces narrow pulse signals.

Table 1
The Timing Performance of GCXT

Parameter	Value
Energy range	3–20 keV
Count rate	0–1 Mcps
Time jitter	< 0.2 μs
Time delay	< 0.2 μs

matches the input pulse profile, indicating that the GCXT exhibits excellent timing performance.

3.2. The 100 m X-Ray Test Facility

The 100 m X-ray test facility (Wang et al. 2023) comprises a vacuum chamber, movable stages, a 100 m tube and the GCXT, as illustrated in Figure 5. The GCXT is placed at one end of the 100 m tube. This tube serves as a conduit connecting the vacuum chamber and the GCXT, enabling the X-rays emitted by the GCXT to form a quasi-parallel beam. Inside the vacuum chamber, the FXT is mounted on a movable stage, facilitating precise alignment with the quasi-parallel X-ray beam. The X-ray photons produced by the GCXT travel through the 100 m tube and are focused onto the FXT detector by the mirror assembly. The FXT subsequently records the position, time, and energy information of the incoming X-ray photons for analysis and calibration.

4. Time Resolution

To accurately determine the time resolution of FXT, it is essential to generate extremely narrow X-ray pulse signals. To address this requirement, we specifically produced X-ray pulse

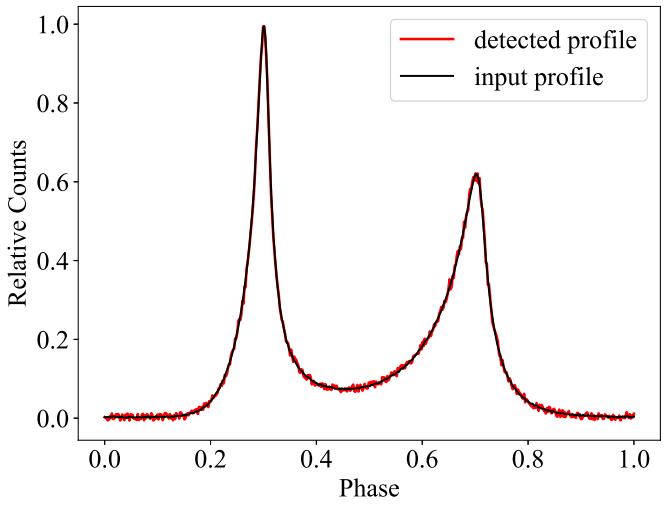

Figure 4. The detected profile of the SDD in response to an input signal featuring a Crab-like profile with a period of 1 ms.

signals with a width of 2.8 μs and a period of 1 ms using a voltage pulse generation module integrated with the GCXT. By generating these X-ray pulse signals, we aimed to test and evaluate the time resolution of both FXT-A and FXT-B under conditions where the pulse signals are significantly narrower. This approach enables a more precise assessment of the time resolution capabilities of the FXT system.

The testing flux of FXT-A and FXT-B is approximately 15 counts s^{-1}, with a duration exceeding 5 hr. To analyze these simulated X-ray signals and determine their periods, we employed the epoch-folding method (Leahy 1987). By dividing the period into 1024 phase bins and allocating events to the corresponding bins based on their timing information, we calculated the χ^2 value. The period corresponding to the maximum χ^2 value was identified as the detected period. This process enabled us to accurately determine the periods of the simulated X-ray signals.

The detected period for both FXT-A and FXT-B was determined to be 1 ms, consistent with the generated X-ray pulse signal. Following this determination, the detected profile can be obtained by folding the entire light curve using the identified period. The detected profiles of FXT-A and FXT-B are illustrated in Figures 6 and 7, respectively. In comparison to the input profile, both FXT-A and FXT-B detected profiles exhibit wider peaks. Given that the width of the input X-ray pulse is negligible, the Full Width at Half Maximum (FWHM) of the detected profile is utilized to characterize the time resolution of FXT. The measured time resolution of FXT-A is 45.6 ± 2.7 μs, while for FXT-B it is 47.1 ± 2.8 μs. These measured time resolutions align with expectations, reflecting the ability of FXT-A and FXT-B to accurately resolve narrow X-ray pulse signals and demonstrating their effective performance in capturing high-resolution temporal features.

5. Pulsar Profile Detection

In a mission dedicated to time-domain X-ray astronomy, detecting pulsar profiles is one of the key tasks. Utilizing the GCXT, we generated simulated X-ray signals that mimic the Crab pulsar profile with a period of 33.6 ms. Since all known pulsar periods exceed 1 ms, we also produced simulated X-ray signals with various periods (5, 2, 0.5, and 0.25 ms for both FXT-A and FXT-B, as well as 10 and 1 ms for FXT-A only) to evaluate the FXT's performance under different conditions. The mean flux and testing duration for these periods are listed in Table 2. The epoch-folding method was employed to search for the period of the X-ray pulse signal. We divided the period into 1024 phase bins and calculated the χ^2 values for different periods to identify the period corresponding to the maximum χ^2 value.

The relative timing accuracy (RTA) is defined as the difference between the detected period and the input period, divided by the input period. Mathematically, this can be expressed as

$$\mathrm{RTA} = \frac{P_{\mathrm{detected}} - P_{\mathrm{input}}}{P_{\mathrm{input}}}, \quad (1)$$

where P_{detected} is the detected period and P_{input} is the input period of the GCXT. This metric quantifies the accuracy of the period detection process by measuring the relative error between the detected period and the known input period, thereby providing valuable insights into the timing performance of FXT. The RTA values are illustrated in Figure 8. It is observed that for both FXT-A and FXT-B, the RTA remains better than 5×10^{-9} across the period range of 0.25–33.6 ms. Using the test data, we employed the bootstrap method to estimate the statistical error of the RTA as a function of the photon numbers. The results are presented in Figure 9. The RTA indicates that the period detection accuracy of FXT is highly precise within the range of 0.25–33.6 ms, demonstrating its overall effectiveness in detecting pulsar profiles with varying periods.

Following the determination of the period, the detected profile can be obtained by folding the entire light curves using the identified period. The profiles detected by FXT-A and FXT-B are displayed in Figures 10 and 11, respectively. Notably, when the period is 33.6 ms, the detected profile closely resembles the input profile of the GCXT. However, as the period decreases, the shape of the profile gradually distorts. To quantitatively evaluate this distortion, Pearson's correlation coefficient is employed as a compression-based method to quantify the similarity between the input and detected profiles (Aghabozorgi et al. 2015). The results are summarized in Table 3. For periods greater than 1 ms, the Pearson's correlation coefficient exceeds 95%, indicating a high level of consistency between the detected and input profiles. However, as the period decreases below 1 ms, the Pearson's

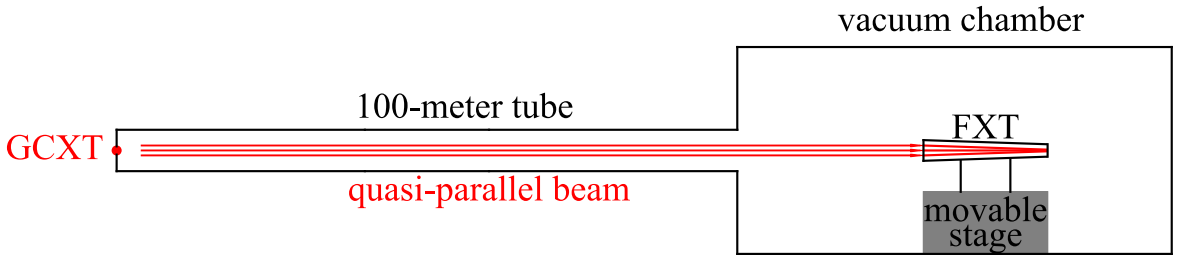

Figure 5. The schematic diagram of the 100 m X-ray test facility.

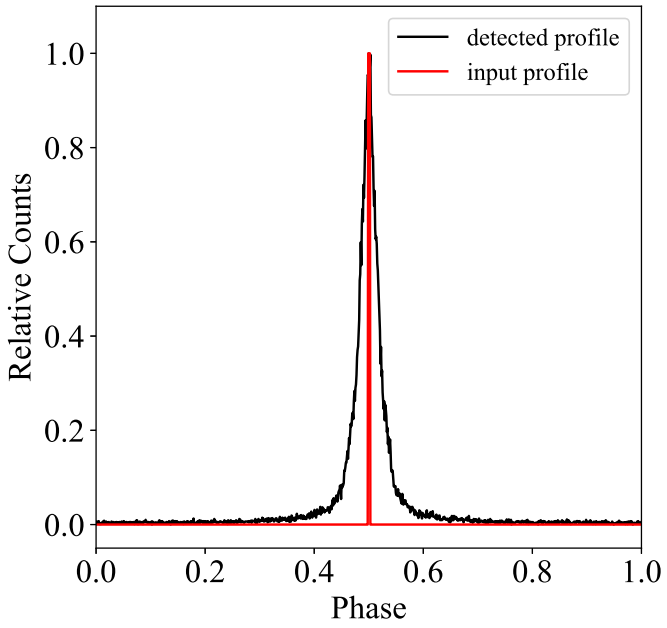

Figure 6. The detected profile for FXT-A.

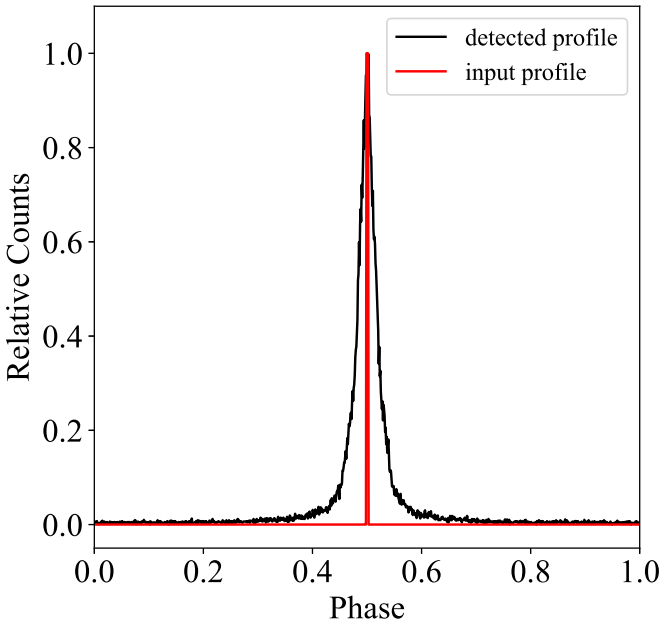

Figure 7. The detected profile for FXT-B.

correlation coefficient gradually diminishes due to the influence of time resolution, leading to a reduction in similarity between the detected and input profiles.

6. Absolute Timing Calibration

Absolute timing calibration for FXT-B was conducted on the ground using the GCXT in conjunction with a voltage generation module to produce X-ray pulse signals with a width of 2.8 μs and a period of 1 ms. Accurately recording the X-ray pulse signal generation time is crucial for precise absolute timing calibration. The voltage generation module begins generating voltage pulses upon detecting the rising edge of the signals provided by the GPS-disciplined rubidium clock, which are then converted into X-ray pulses through the GCXT. After detecting the falling edge, the output of the X-ray pulse signals is terminated. A time interval analyzer was utilized to record the times of the rising and falling edges. Therefore, we consider the time of the rising edge to be the start time of the pulse signal, and the time of the falling edge to be the end time. Due to the extremely narrow pulse signal relative to the time resolution of FXT, we take the average of the start and end times as the pulse time.

Table 2
The Mean Flux and Testing Duration for Different Periods

FXT	Period (ms)	Mean Flux (counts s^{-1})	Testing Duration (s)
FXT-A	33.6	176	7500
	10	180	7500
	5	172	7500
	2	184	7500
	1	191	7500
	0.5	174	7500
	0.25	185	7500
FXT-B	33.6	226	7500
	5	229	7500
	2	230	7500
	0.5	234	7500
	0.25	231	7500

The epoch-folding method was employed to determine the period of the X-ray signals detected by FXT-B. This period was

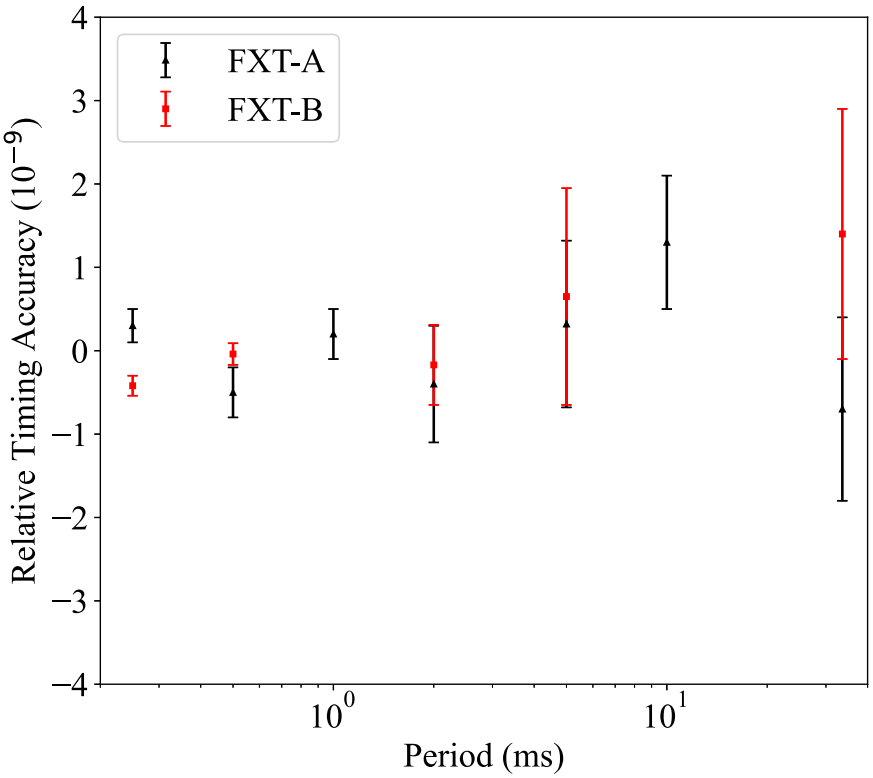

Figure 8. The RTA for FXT-A and FXT-B.

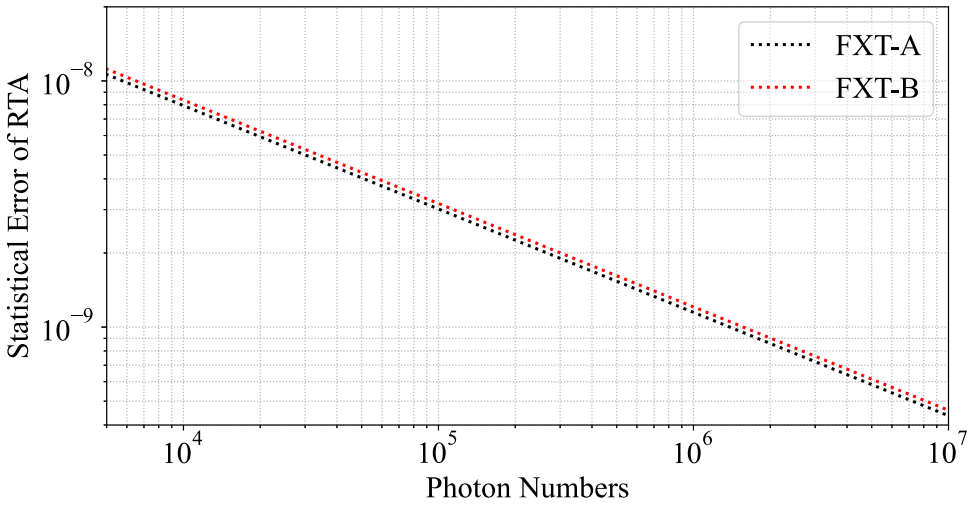

Figure 9. The statistical error of the RTA as a function of the photon numbers.

ultimately confirmed to be 1 ms, which is consistent with the input pulse period. Subsequently, the light curve was folded based on the determined period to obtain the profile (see Figure 7). By fitting the peak position of the profile, we determined the arrival time of the X-ray pulses.

We conducted multiple tests on the arrival times of the X-ray pulses. The absolute timing of input pulses was recorded using a time interval analyzer. After this, we calculated the arrival times of the X-ray pulses observed by FXT-B. The time delays between the input pulses and the observed pulses are depicted in Figure 12. The mean time delay was measured to be 4.4 ± 2.1 μs. Several factors contribute to this mean time delay. First, there is a time interval of 0.15 μs between the appearance of the PPS signal and the generation of the voltage pulse in the

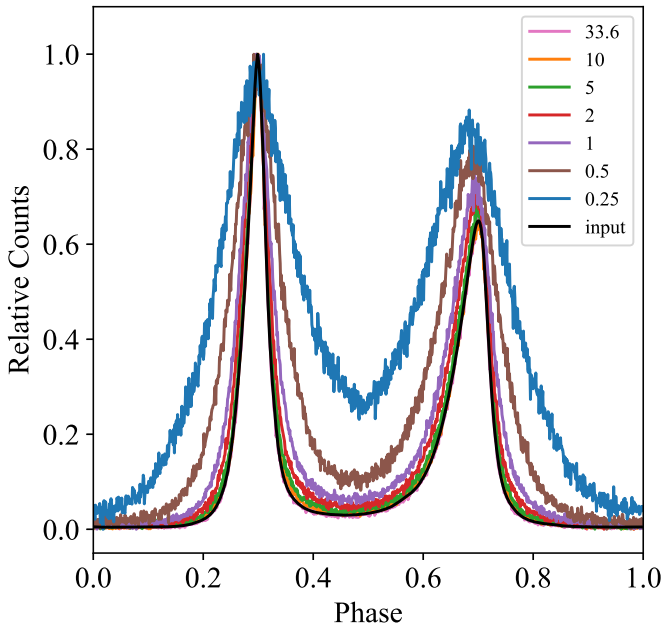

Figure 10. The detected profiles for FXT-A.

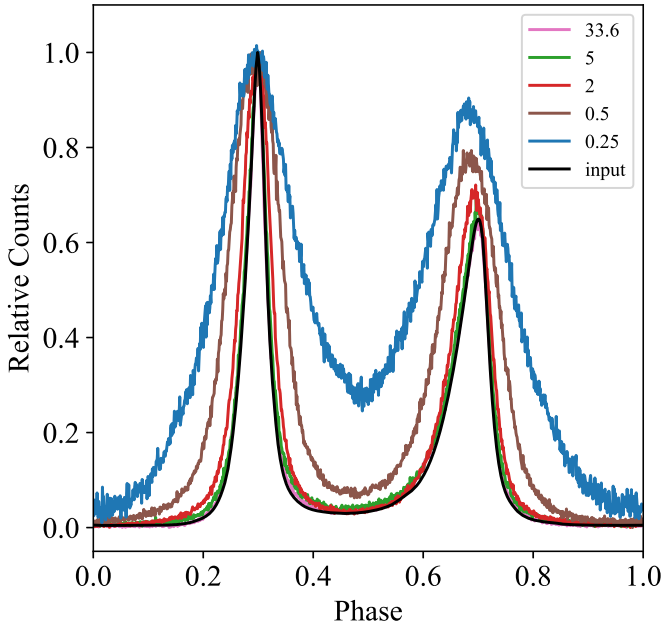

Figure 11. The detected profiles for FXT-B.

voltage pulse generation module, which accounts for part of the observed delay. Second, the propagation of photons introduces an additional time delay. The distance between the GCXT and the detector is 105 m, resulting in a time delay of 0.35 μs due to the finite speed of light. Considering these two time delays, the time delay of FXT-B is 3.9 ± 2.1 μs, characterizing the time response of FXT-B.

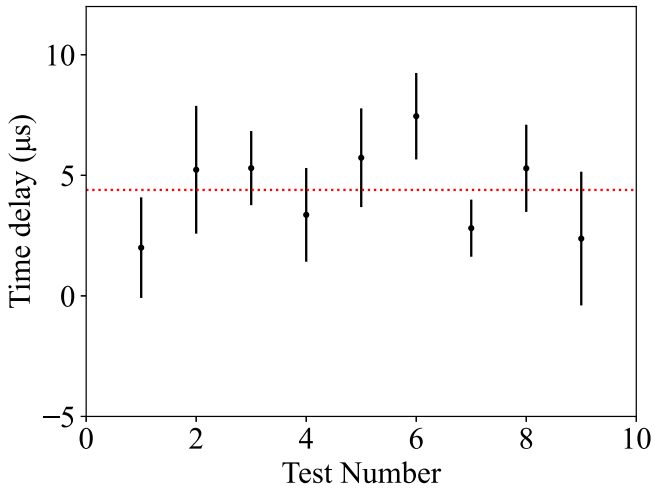

Figure 12. The time delay between input pulses and observed pulses was measured in nine independent tests. Each data point represents the result of a single test, while the red line signifies the average of these nine results.

Table 3
The Pearson's Correlation Coefficients Between the Detected and Input Profiles

Period (ms)	FXT-A	FXT-B
33.6	99.95%	99.94%
10	99.91%	
5	99.83%	99.81%
2	99.22%	99.19%
1	97.66%	
0.5	90.47%	89.59%
0.25	79.45%	78.76%

7. Conclusions

Before the launch, we conducted extensive tests on the timing performance of the FXT. By generating simulated X-ray signals with various periodic Crab-like profiles using the GCXT equipped with a pulsar simulation module, we determined that the relative time accuracy of the FXT is superior to 5×10^{-9} within the period range of 0.25–33.6 ms. Additionally, for periods exceeding 1 ms, the Pearson's correlation coefficient between the detected profile and the input profile was found to be greater than 95%.

By utilizing the GCXT in conjunction with the voltage pulse generation module, we created a pulse signal with a width of 2.8 μs and a period of 1 ms to assess the time resolution of the FXT. The time resolution was determined to be 45.6 ± 2.7 μs for FXT-A and 47.1 ± 2.8 μs for FXT-B. An absolute timing calibration for FXT-B was conducted using the GCXT and a time interval analyzer. The time delay between the detected pulse and input pulse was determined to be 3.9 ± 2.1 μs.

The excellent timing performance of the FXT enables it to conduct fast X-ray timing observations. While in orbit, the timing performance of FXT (absolute timing of FXT-A) can be further calibrated through observations of pulsars such as the Crab pulsar.

Acknowledgments

This study is supported by the Strategic Priority Research Program on Space Science, the Chinese Academy of Sciences, grant No. XDA15310103.

References

Aghabozorgi, S., Shirkhorshidi, A. S., & Wah, T. Y. 2015, Inf. Syst., 53, 16
Arcangeli, L., Borghi, G., Bräuninger, H., et al. 2017, Proc. SPIE, 10565, 1056558
Bachetti, M., Markwardt, C. B., Grefenstette, B. W., et al. 2021, ApJ, 908, 184
Chen, C. 2022, PhD thesis, Univ. Chinese Academy of Sciences, China
Chen, C., Xiao, S., Xiong, S., et al. 2021, ExA, 52, 45
Chen, Y., Cui, W., Han, D., et al. 2020, Proc. SPIE, 11444, 114445B
Chen, Y., Sun, X., Li, Z., et al. 2022, ApOpt, 61, 8813
Cordes, J. M., & Chatterjee, S. 2019, ARA&A, 57, 417
Cui, W., Wang, H., Zhao, X., et al. 2023, ExA, 55, 603
Friedrich, P., Bräuninger, H., Budau, B., et al. 2008, Proc. SPIE, 7011, 70112T
Friedrich, P., Stieglitz, V., Burwitz, V., et al. 2024, AcAau, 221, 255
Gezari, S. 2021, ARA&A, 59, 21
Harding, A. K. 2022, in Astrophysics and Space Science Library, ed. S. Bhattacharyya, A. Papitto, & D. Bhattacharya, Vol. 465 (Cham: Springer), 57
Kuiper, L., Hermsen, W., Walter, R., & Foschini, L. 2003, A&A, 411, L31
Leahy, D. A. 1987, A&A, 180, 275
Li, Y., Wen, X., Sun, X., et al. 2020, SSPMA, 50, 129508
Martin-Carrillo, A., Kirsch, M. G. F., Caballero, I., et al. 2012, A&A, 545, A126
Meidinger, N., Andritschke, R., Dennerl, K., et al. 2021, JATIS, 7, 025004
Molkov, S., Jourdain, E., & Roques, J. P. 2010, ApJ, 708, 403
Rots, A. H., Jahoda, K., & Lyne, A. G. 2004, ApJL, 605, L129
Sunyaev, R., Arefiev, V., Babyshkin, V., et al. 2021, A&A, 656, A132
Terada, Y., Enoto, T., Miyawaki, R., et al. 2008, PASJ, 60, S25
Tuo, Y., Li, X., Ge, M., et al. 2022, ApJS, 259, 14
Wang, Y., Zhao, Z., Hou, D., et al. 2023, ExA, 55, 427
Xiao, S., Liu, Y.-Q., Gong, K., et al. 2024, ApJS, 270, 3
Xiao, S., Liu, Y. Q., Peng, W. X., et al. 2022, MNRAS, 511, 964
Yang, Y., Wang, Y., Han, D., et al. 2023, ExA, 55, 625
Yuan, W., Zhang, C., Chen, Y., et al. 2018, SSPMA, 48, 039502
Yuan, W., Zhang, C., Chen, Y., & Zhixing, L. 2024, The Einstein Probe Mission, Handbook of X-ray and Gamma-ray Astrophysics (Singapore: Springer Nature Singapore), 1171
Zhang, Y., Li, W., Luo, L., et al. 2024, ExA, 57, 28
Zhao, D., Zhang, C., Ling, Z., et al. 2018, Proc. SPIE, 10699, 106995N
Zhao, X., Xu, J., Cui, W., et al. 2024, PASP, 136, 105001
Zhou, F., Wu, G., Zhao, B., et al. 2013, AcPSn, 62, 119701